RESEARCH ARTICLE

Design and Implementation of an Isolated Bidirectional Phase-Shift Full-Bridge Converter With High Transformation Ratio

SEN-TUNG WU AND BO-YU YANG

Innovative Energy Lab, Department of Electrical Engineering, National Formosa University, Yunlin 632301, Taiwan

Corresponding author: Sen-Tung Wu (stwu@nfu.edu.tw)

ABSTRACT In this paper, a bidirectional full-bridge phase-shift converter with high transformation ratio scheme is proposed. The main architecture of this converter is dual active full-bridge circuit. By using phase-shift modulation, the energy can be transmitted between high-voltage-side and low-voltage-side, and also can make the power switches have the function of soft-switching. This converter is designed with the transmission power of 1kW and the digital signal processor TMS320F28335 is utilized as the main system controller core. Finally, it realizes the bidirectional power conversion mechanism between battery 50 V_{dc} and DC grid 400 V_{dc}. The experimental results show that the maximum conversion efficiency of this converter when operating in the forward charging mode (G2V mode) is up to 92.25 %, and in the reverse discharging mode (V2G mode), the maximum conversion efficiency is up to 93.02 %. In comparison with the related studies for dual active full-bridge converters, the conventional transformation ratio is lower or equal to 4. This study with high transformation ratio can reach 8 for practical high-low voltage bidirectional applications. After the validation for both modes, the proposed concept is practical in the high transformation scenarios.

INDEX TERMS Bidirectional full-bridge converter, phase-shift modulation, zero voltage switching, high transformation ratio, DAB.

I. INTRODUCTION

In recent years, the integration of electric vehicle (EV) and power grids has gradually become new discussion issues [1], [2], and the characteristics of electric vehicles are reducing the consumption of petrochemical energy and carbon emissions. Electric vehicle contains battery packs and supercapacitors within. The stored energy in an EV can be regarded as a movable energy storage tank [3], [4]. Hence, the applications of electric vehicles are trends from the past few years till now [5]. The bidirectional power flow technique of G2V (grid to vehicle)/V2G (vehicle to gird) is one of the EV applications. The concept of G2V/V2G is shown in Fig. 1. This technology can help the power grid balance the load in different time periods, such as "Valley filling" and "Peak shaving" power management methods [6], [7]. The concept

The associate editor coordinating the review of this manuscript and approving it for publication was N. Prabaharan.
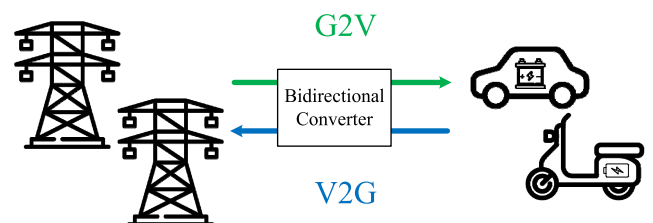

FIGURE 1. Basic concept of V2G and G2V.

of valley filling is that when the power demand from user is less in the night, the power grid will charge to electric vehicles with redundant electricity [8], [9]. On the other hand, the concept of peak shaving is that if the power gird has electricity requirement in day time, EVs with full or partial electricity in parking spaces can discharge to the power grid to meet the higher power demand temporarily. Peak load adjustment allows the power station companies to maintain the stability of electricity, and provide power grids through

the energy storage device to meet temporary power require-ments. These devices and equipment will be integrated with smart bidirectional power meters [10]. The energy from EVs can be measured and calculated through the meters as an income profit by selling the electricity back to the power grid. Hence, the bidirectional power converter is a basic scheme to compensate the shortage between the power demand of the grid and EVs.

The specifications of this study will be determined by the most common electric scooter batteries for commercial transportation [11]. In general, the standard battery voltage of the electric scooter is set for 48 V [12]. Thus, the out-put voltage for low-voltage side is chosen for 50 V (2 V higher for practical charger output design). The main archi-tecture of electric scooter charger circuit in commercial is usually flyback converter. The features of flyback converter are shown below: 1. low price cost; 2. fewer component account; 3. good electrical isolation; 4. suitable for multiple output loads applications. However, the power level of fly-back converter is usually in low range (under 100 W), and the flyback scheme is not suitable for bidirectional energy delivery applications [13]. Therefore, this study will focus on a bidirectional full-bridge phase-shift converter as a main architecture to achieve the function of bidirectional energy transmission [14], [15], [16].

In some DAB applications, the transformation ratio is still in low range for 1, 2, and even equal to 4. For example, [17] provided a hybrid mode modulated DAB converter which the output voltage can be increasing or decreasing. The input voltage is 80 V_{dc}, and the output voltage is 40 V_{dc}, 80 V_{dc}, and 100 V_{dc}. The transformation ratio is from 1.25 to 2. For reference [18], the DAB operated in a 1.5 kW micro grid to energy storage system. The input voltage is set for 140V_{dc}, and the output voltage is set for 70 V_{dc}. In this bidirectional power delivery scenario, the transformation is 2. According to these references, the transformation ratio is still low. For reference [19], this study gave a multiple input-series-output-series (ISOS) DAB modular converters for DC grid application. Each modular has input voltage for 150 V_{dc}, and the output voltage is 150 V_{dc}. The transforma-tion is 1 and the benefit of this modularized DAB also has series-resonant characteristics to achieve the soft-switching function. For reference [20], hybrid-bridge DAB converter and hybrid modulation-based was adapted to a wide voltage range. In this study, the input voltage is 300 V_{dc} of the DC bus, and the output voltage is 100-200 V_{dc} for energy storage system. The transformation is 1.5-3. In Table 1, the input/output voltage, the transformation ratio, the power level are compared.

In this study, the high voltage is set for 400 V from DC grid, and the low voltage is set for 50 V from elec-tric scooter's battery. The power level is set for 1 kW to verify the feasibility of the proposed novel structure. The future goal is to implement a charging-discharging mecha-nism and application between DC grid and electric scooters bi-directionally [21], [22], [23], [24].

TABLE 1. The comparison for the state-of-the-art works.

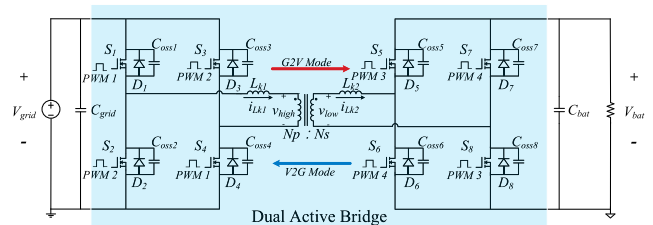| Reference	Input/Output Voltage (V_{dc})	Transformation Ratio	Power Level of DAB
[17]	80/40-100	1.25-2	550 W
[18]	140/70	2	1.5 kW
[19]	150/150	1	600 W
[20]	300/100-200	1.5-3	500 W
Proposed study	400/50	8	1 kW

FIGURE 2. Architecture of the proposed circuit.

To outline the design procedure of this study, the paper will be discussed as the following sections. The proposed structure and the operation principles are analyzed in section II. In Section III, the circuit specifications and design pro-cedure are provided in detail. Also the magnetic component design is involved. After the key components are determined, the experimental results for V2G and G2V are demonstrated in Section IV. In this section, the key waveforms are mea-sured to verify the proposed scheme. In the end of the work, Section V will summarize the contribution from this study and further related researches.

II. PROPOSED SCHEME AND OPERATION PRINCIPLE

This paper proposed and implemented a bidirectional full-bridge phase-shift converter with high-voltage ratio, which is shown in Fig. 2. This paper defines the forward charging mode (G2V Mode→ V_{grid} delivers the energy to V_{bat} as red direction) to provide the energy to the battery of the electric scooter. For the other mode, that is, the reverse discharging mode (V2G mode→ V_{bat} delivers the energy to V_{grid} as blue direction) which supplies the energy from the battery to DC grid reversely. The proposed circuit is evolved from the conventional one-way phase-shift converter, and the rectifier diodes of the output side are replaced by the power switches. Hence, the dual active bridge (DAB) is used as the main architecture, and the bidirectional energy conversion can be achieved successfully. In such a bidirectional power flow control, the digital signal processor (DSP) is necessary as a main controller to enhance system stability and reliability.

For the control strategy, the control mechanism in this paper utilizes single-phase-shift (SPS) control method, and
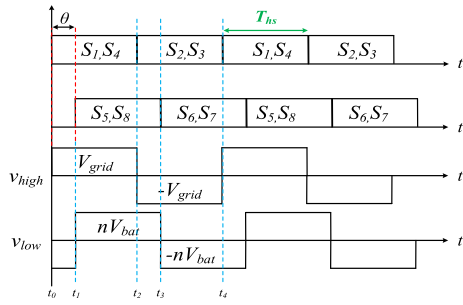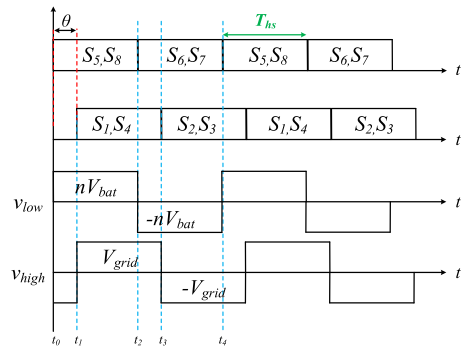
FIGURE 3. Timing Diagram of SPS (G2V mode).

FIGURE 4. Timing Diagram of SPS (V2G mode).

FIGURE 5. The theoretical waveforms of G2V mode.

FIGURE 6. The current path of State I.

SPS control is the simplest control method of the DAB architecture, and it is also the most applicable. As shown in Fig. 3 and Fig. 4, in the SPS control, the diagonal switches are driven by the complementary signals. The duty cycle of the driving signal is set for almost 50 % (ignore the dead time and the conduction voltage of each power switch to simplify the analysis). The square wave voltage at the primary side and the secondary side of the transformer are V_{low} and V_{high}. The driving signals of these 8 switches exist a phase-shift ratio D ($\theta/180$), and there is also a phase-shift time between V_{high} and V_{low}. DT_{hs} is a cycle of half a PWM driving signal. For the power flow direction of different power sources, the phase-shift sequence between V_{high} and V_{low} is also reversed, and the power flow direction always passes from the phase lead side to the phase lag side.

Based on Fig.3 and Fig.4, the control method of this DAB is that if the phase shift angle θ increases (v_{high} leads v_{low}), the output power will be higher in G2V mode. Once θ decreases, the output power will be lower. Conversely, if the DAB operates in V2G mode, the phase shift angle θ is still a factor to regulate the power level, but phase shift angle of v_{low} must lead v_{high} for sure. In brief, the phase shift angle is to adjust the power demand from the output, and the angle leading side will deliver the energy to the lagging side. In this study, the DAB structure has the feature of soft switching, so that the power switch can realize the soft switching function in both power flow directions when the load level is greater than a certain level. Fig. 5 shows the theoretical waveform of the converter operating in G2V mode. Depending on the power switch switching state, the circuit can be divided into eight
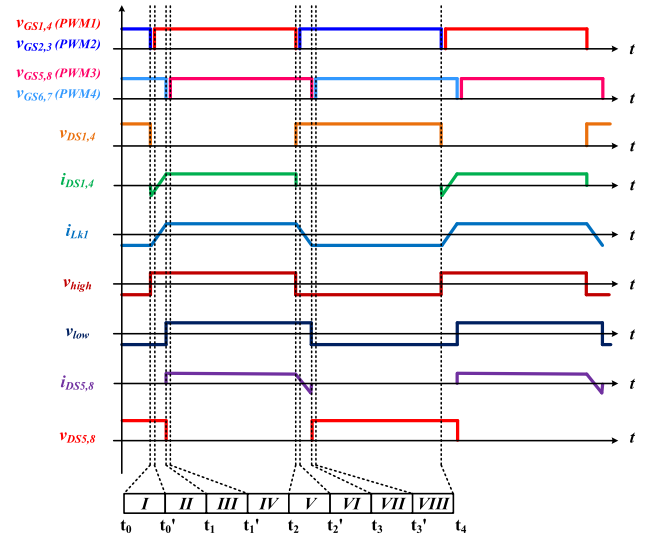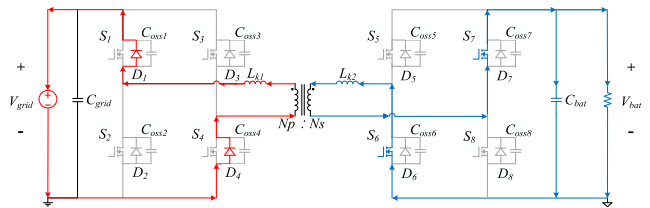
operating modes. The G2V and V2G mode are almost the same operation concepts, thus, the G2V mode is analyzed only.

A. STATE I ($t_0 < t \leq t_0'$)
As shown in Fig. 6, the power switches $S_1 \sim S_4$ are in the cut-off state during this operation state, and the inductor current forms a continuous flow path through the power switches' body diodes D_1 and D_4, so that the high-voltage side power switches S_1 and S_4 achieve the condition of zero-voltage switching. At the same time, the low-voltage side power switches S_6 and S_7 are turned on, so the energy will be transferred to the battery through S_6 and S_7. When S_1 and S_4 enter the next working state and turn on, the power switch can realize the function of zero-voltage switching.

B. STATE II ($t_0' < t \leq t_1$)
As shown in Fig. 7, since the parasitic capacitors C_{oss1} and C_{oss4} have already released the energy to zero in the previous operation state, the power switches S_1 and S_4 can achieve the function of ZVS at the beginning of this operation state, and the low-voltage side output capacitor C_{bat} is looped through S_6 and S_7 until t = t_1, when this state finishes.

C. STATE III ($t_1 < t \leq t_1'$)
As shown in Fig. 8, when t = t_1, S_1 and S_4 at the high-voltage side are still turned on; while the low-voltage side enters the
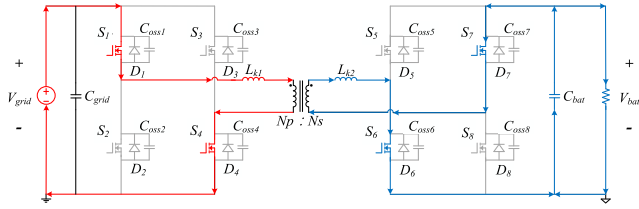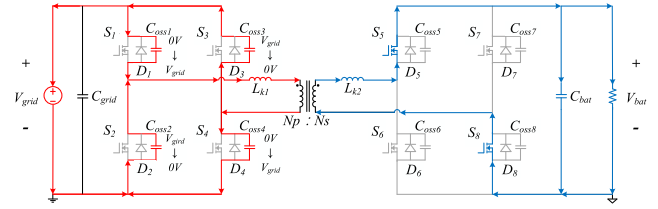
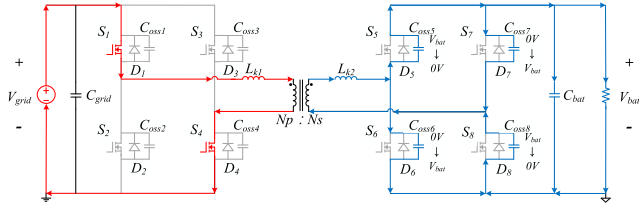**FIGURE 7.** The current path of State II.

FIGURE 8. The current path of State III, (C_{oss} charging & discharging).

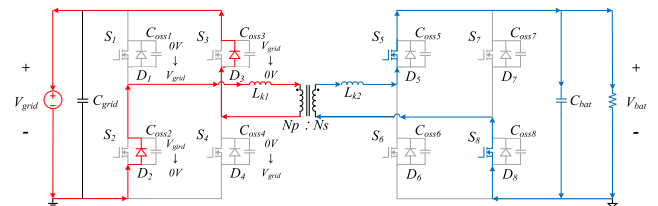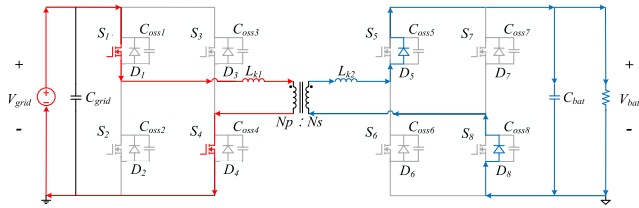**FIGURE 9.** The current path of State III, (body diode on).

FIGURE 10. The current path of State IV.

FIGURE 11. The current path of State V, (C_{oss} charging & discharging).

FIGURE 12. The current path of State V, (body diode on).
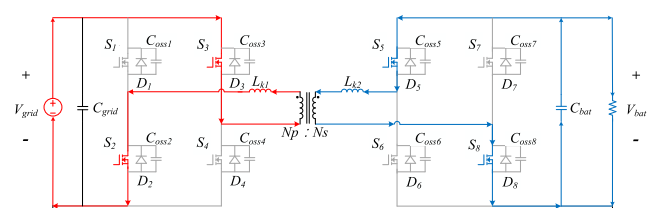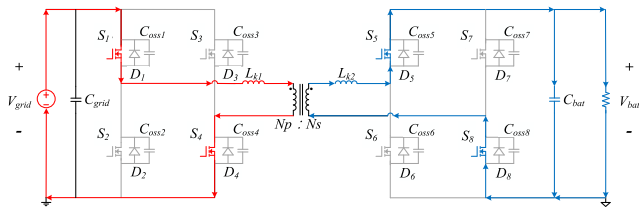

FIGURE 13. The current path of State VI.

dead time, the power switches $S_5 \sim S_8$ are in the cut-off state during this operation state. When the voltage of C_{oss5} and C_{oss8} decrease to zero and the voltage of C_{oss6} and C_{oss7} are being charged to V_{bat}, the current will continue to provide energy to the battery through the body diodes D_5 and D_8. The current state is shown in Fig. 9.

D. STATE IV ($t'_1 < t \leq t_2$)
As shown in Fig. 10, the high-voltage side power switches S_1 and S_4 are still turned on. Because the parasitic capacitors C_{oss5} and C_{oss8} have already released the energy to zero during the previous operation state, so the power switches S_5 and S_8 can achieve the function of ZVS at the beginning of this operation state. Therefore, the energy will be transferred to the battery side through power switches S_1, S_4, S_5 and S_8.

E. STATE V ($t_2 < t \leq t'_2$)
As shown in Fig. 11, when t = t_2, the low voltage side S_5 and S_8 are still on; while the high voltage side enters the dead time, the power switches $S_1 \sim S_4$ are cut-off at

this state. When C_{oss2} and C_{oss3} voltages drop to zero and C_{oss1} and C_{oss4} voltages are charged to V_{grid}, the current will continue to excite the transformer and transfer energy to the low-voltage side through the body diodes D_2 and D_3. The current path is shown in Fig. 12.

F. STATE VI ($t'_2 < t \leq t_3$)
As shown in Fig. 13, since the parasitic capacitors C_{oss2} and C_{oss3} have already released the energy to zero in the previous operation state, the power switches S_2 and S_3 can achieve the function of ZVS at the beginning of this operation state, and the low-voltage output capacitor C_{bat} is looped through S_5 and S_8 until t = t_3, when this operation state ends.

G. STATE VII ($t_3 < t \leq t'_3$)
As shown in Fig. 14, when t = t_3, the high voltage side S_2 and S_3 are still on; while the low voltage side enters the dead time, the power switches $S_5 \sim S_8$ are cut-off at this state. When the voltage of C_{oss6} and C_{oss7} drops to zero and the voltage of C_{oss5} and C_{oss8} is charged to V_{bat}, the current will continue to supply energy to the load side through the body diodes D_6 and D_7. The current path is shown in Fig. 15.

H. STATE VIII ($t'_3 < t \leq t_4$)
As shown in Fig. 16, the high voltage side power switches S_2 and S_3 are still on, while the parasitic capacitors C_{oss6} and C_{oss7} have already lowered the voltage to zero during the previous operating phase, so the power switches S_6 and S_7 can
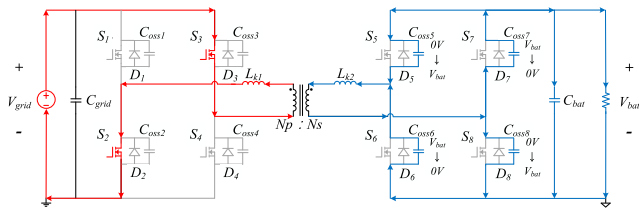
FIGURE 14. The current path of State VII, (C$_{oss}$ charging & discharging).
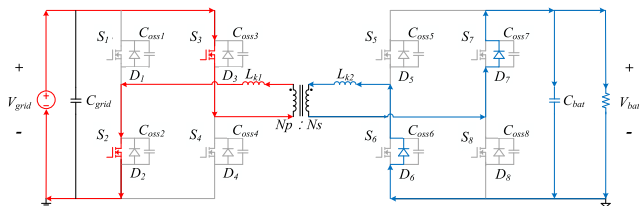

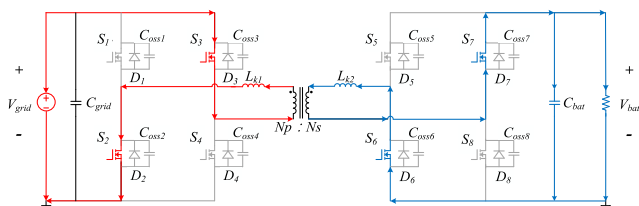**FIGURE 15.** The current path of State VII, (body diode on).

FIGURE 16. The current path of State VIII.

achieve the function of ZVS at the beginning of this operating phase. Therefore, the energy will be transferred from power switches S_2, S_3, S_6 and S_7 to the load side. At this point, the G2V mode has completed a complete switching cycle.

III. CHARACTERISTICS OF POWER TRANSMISSION

The characteristic curve of the transmitted power with varying phase-shift ratio is shown in Fig. 17, and the per-unit value of the transmitted power is shown in Eq(1).

$$P = N \cdot V_{gird} \cdot V_{bat} / \left(8 \cdot f_s \cdot L_{eq1} \right) \quad (1)$$

where N is the transformer turns ratio, (N_{high}/N_{low}), L_{eq1} is the equivalent leakage inductance at the high voltage side, and f_s is the switching frequency. From this figure, the general rule of DAB, and the following considerations are necessary for the design of DAB.

1). The transmitted power is sinusoidal which is related to the phase-shift ratio D. The graph is symmetric at $D = 0.5$.

2). The zero and maximum points of the transmitted power are located at $D = 0$ and $D = 0.5$, respectively.

3). When $D < 0.5$, the transmitted power increases with the increase of phase-shift ratio D; when $D > 0.5$, the transmitted power decreases.

4. When the direction of the power flow changes, the rule is the same as above.

Eq(2) is the relationship between the transmitted power, where N is the transformer turns ratio, L_{eq1} is the equivalent leakage value on the high-voltage side, f_s is the operating frequency, T_{hs} is the half-cycle time length ($0.5/f_s$), and D
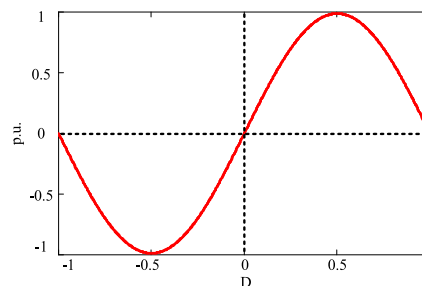

FIGURE 17. Curve of transmitted power with varying phase-shift ratio.

is the phase-shift ratio within half a switching cycle, which is defined as shown in Eq(3), where θ represents the phase difference between the two sides of the transformer. Eq(4) is the maximum transmitted power.

$$P = \frac{N \cdot V_{grid} \cdot V_{bat} \cdot D(1 - D)}{2 \cdot f_s \cdot L_{eq1}} \quad (2)$$

$$D = \frac{\theta}{180}, \quad (0 \leq |D| \leq 1) \quad (3)$$

$$P_{max} = \frac{N \cdot V_{grid} \cdot V_{bat}}{8 \cdot f_s \cdot L_{eq1}} \quad (4)$$

IV. NON-IDEAL CHARACTERISTICS OF POWER TRANSMISSION

In consideration of the actual power delivery, a dead time is added between the PWM drive signals of the same bridge arm to avoid the short circuit damage. Since the G2V mode is the same concept as the V2G mode, the following analysis and description will focus on the non-ideal power transfer characteristics of G2V mode.

From Fig. 18, it can be found that the transmission power and different phase-shift ratio D do not form ideal sinusoidal curves. Due to the existence of dead time, the zero point of transmission power is not at the position of $D = 0$. The larger the value of M, the later the intersection of M curve and ideal curve (red curve) occurs. When the M curve passes the intersection of ideal curve, the transmission power curve will change to ideal curve, and this phenomenon is called phase-drift. This situation usually occurs in the high frequency light load condition, when the dead time is larger, the phase-drift phenomenon is more obvious. Hence, the dead time should be smaller.

According to the definition of M value, it represents the percentage of dead time in the switching cycle, the concept is shown in Fig. 19 and Eq(5).

$$M = \frac{Dead\ Time}{50\%} \quad (5)$$

According to the above phase drift phenomenon, the reference [1] analyzed the relationship between dead time and transmitted power. The relationship is shown in Eq(6). Where T_{hs} represents the half-cycle duration, V_{grid} is the high-side voltage value, L_{eq1} is the high-side equivalent leakage value,
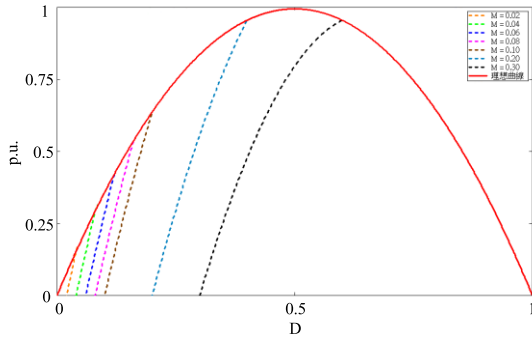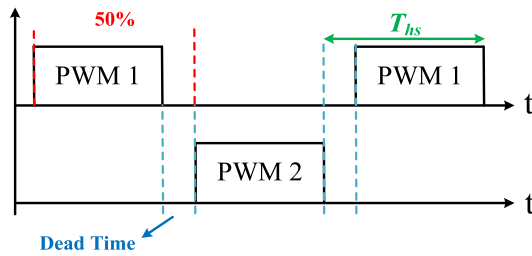
FIGURE 18. Non-Ideal curve of transmitted power.

FIGURE 19. Relationship of *M* and dead time.

TABLE 2. Specifications for the input and output of proposed converter.

Parameters	Specifications
V_{grid}	400 V_{DC}
V_{bat}	50 V_{DC}
fs (Switching frequency)	100 kHz
P (Rated power)	1 kW
D (Phase-shift ratio)	-0.166 ~ 0.166

D is the phase-shift ratio, and M is the dead time ratio.

$$P = \frac{T_{hs} \cdot V_{grid}^2}{4 \cdot L_{eq1}} \cdot [8 \cdot (1-D) \cdot (D-M)] \qquad (6)$$

V. CIRCUIT DESIGN CONSIDERATIONS

In order to reduce the size of the magnetic components and increase the power density of the converter, the power switching frequency is setting for 100 kHz. In this paper, a bidirectional full-bridge phase-shift converter with a rated output of 1 kW and a high transformer ratio enables bidirectional power transfer between the DC grid port and the battery storage port. The specifications of this proposed scheme are shown in Table. 2.

A. DESIGN PROCEDURES OF KEY PARAMETERS

This section introduces the design parameters of the circuit, including the transformer turns ratio N, equivalent leakage value L_{eq1}, switching frequency f_s, and dead time. Besides, the ideal transmission power characteristics mentioned in the above section will be utilized as a design reference to ensure the converter to achieve the required transmission power level. The design flow is shown in Fig. 20.
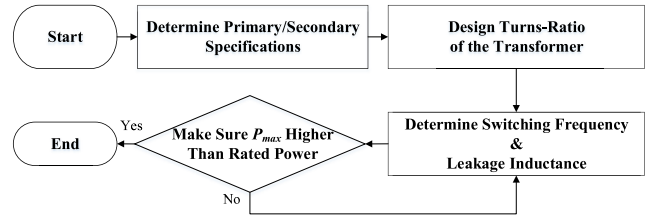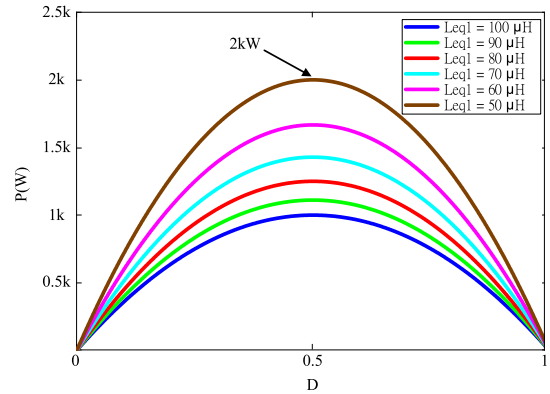

FIGURE 20. Flowchart of design procedure.

FIGURE 21. L_{eq1} V.S. P_{max} (fs = 200 kHz).

B. DESIGN OF TRANSFORMER TURNS RATIO

After determined the converter specifications, the transformer turns ratio was calculated. In order to reduce the circulating power to improve the efficiency, the DC grid port voltage and the storage port voltage are selected as the design criteria and the transformer is designed as shown in Eq(7).

$$N = \frac{N_{high}}{N_{low}} = \frac{V_{grid}}{V_{bat}} = \frac{400}{50} = 8 \qquad (7)$$

C. CHOOSE LEAKAGE INDUCTANCE, SWITCHING FREQUENCY

The transfer power characteristic analysis mentioned in the previous section is used as the design criterion for this converter, and the selection of the transfer power curve will be carried out. First, setting an operating frequency f_s, then substitute it into Eq(2), and observe the maximum power affected by different leakage inductance values L_{eq1}. Fig. 24, Fig. 25, and Fig. 26 show the relationship between the leakage inductance and the transmitted power. It can be found that when the operating frequency f_s is a fixed value, the greater the leakage inductance value L_{eq1}, the lower the maximum achievable transmission power level; conversely, the smaller the leakage inductance value L_{eq1} is, the higher the maximum transmission power level will be.

Since all the maximum transmission power in Fig. 26 is much higher than the target transmission power, 50 kHz is still not considered as the switching frequency based on the trade off the size of magnetic components. Most of the curves in Fig. 24 are in line with the target transmission power, but the switching loss will increase if the switching frequency is too high. Hence, 200 kHz is not considered as the switching
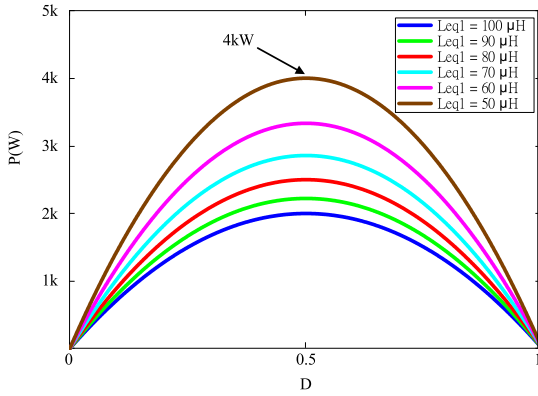
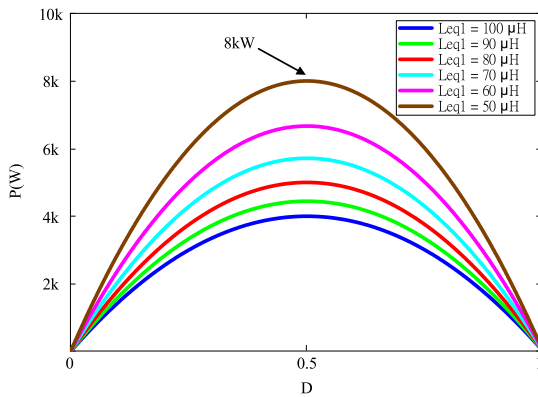**FIGURE 22.** L_{eq1} V.S. P_{max} (fs = 100 kHz).

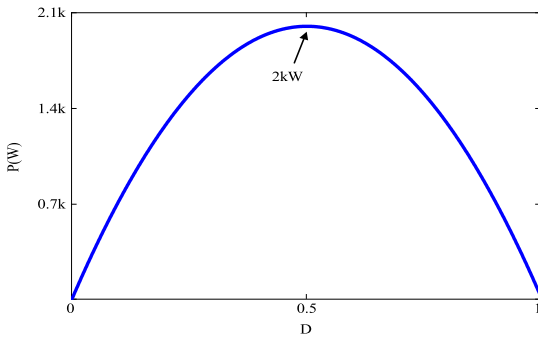**FIGURE 23.** L_{eq1} V.S. P_{max} (fs = 50 kHz).

FIGURE 24. Practical transmitted power curve with phase-shift ratio.

frequency. Consequently, 100 kHz was properly selected as the switching frequency of the converter. After the switching frequency is determined, the equivalent leakage inductance L_{eq1} can be selected as well. The target transmitted power is usually set at $\frac{1}{2} \sim \frac{2}{3}$ of the peak power, so the equivalent leakage inductance is 100 μH, and finally the transmission power curve was plotted as shown in Fig. 27.

After the leakage inductance and the switching frequency are determined, the next step is to design the duration of the dead time. The length of the dead time is the key to achieve zero voltage switching of the power switches. If the dead time is too short, the leakage current will not be able to release
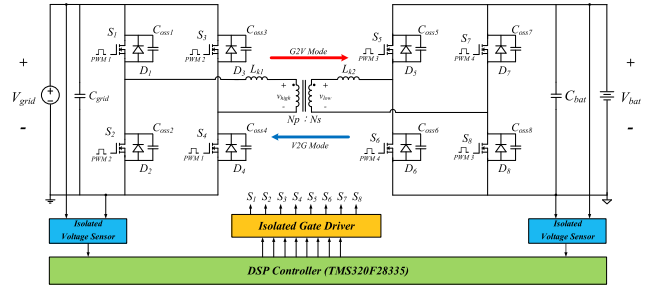

FIGURE 25. Complete digital control diagram with DSP controller.

the energy stored in the parasitic capacitor C_{oss} within the dead time, which will cause the zero voltage switching to fail and increase the switching losses. In order to achieve zero-voltage switching successfully, the following equations are helpful to obtain the minimum dead time for this proposed converter. According to Eq(8) and Eq(9), the minimum dead time of this scheme can be calculated, where $C_{OSS_{high}}$ and $C_{OSS_{low}}$ are the stray capacitance of the power switch in high voltage side and low voltage side. $L_{m_{high}}$ and $L_{m_{low}}$ are the magnetizing inductance in high voltage side and low voltage side respectively.

$$t_{dead} \geq 8 \cdot C_{OSS_{high}} \cdot f_s \cdot L_{m_{high}}$$
$$= 8 \cdot 54p \cdot 100k \cdot 1.123m \cong 48.5136ns \quad (8)$$
$$t_{dead} \geq 8 \cdot C_{OSS_{low}} \cdot f_s \cdot L_{m_{low}}$$
$$= 8 \cdot 390p \cdot 100k \cdot 17.93\mu \cong 5.5942ns \quad (9)$$

Since the converter contains two different driving signals at the high-voltage side and low-voltage side, two different minimum dead times are necessary in the calculation above. and the stray capacitance and parasitic inductance in the circuit have not been taken into account. In order to retain the residual margin of dead time, 200 nS is finally chosen as the dead time in this paper.
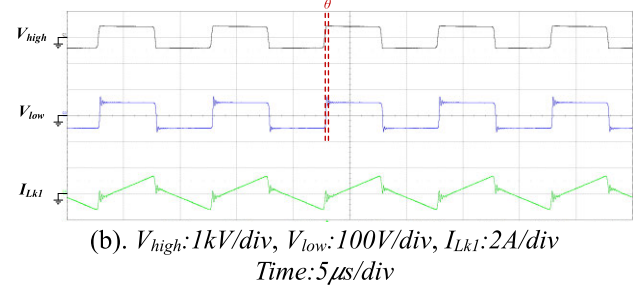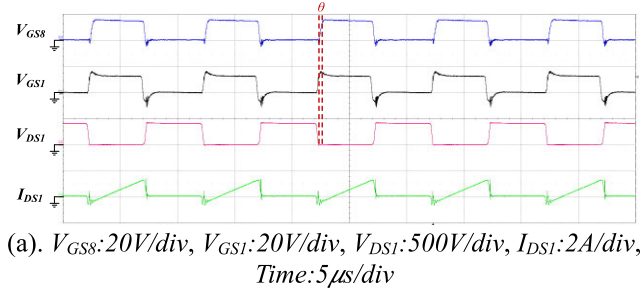
VI. EXPERIMENT AND MEASUREMENT RESULT
A. EXPERIMENT SETUP AND SPECIFICATION
In this section, the experimental testing bench setup and waveform measurements are demonstrated and discussed. The converter is designed according to the circuit parameter design and component selection in the previous section. In terms of driving signals, this structure utilizes TMS320F28335 digital signal processor developed by Texas Instruments as the system control core to realize the bidirectional power regulation between the DC grid port and the energy storage port. As shown in Fig. 28, DSP can not only effectively reduce the size of the circuit, but also increase the stability and reliability of the circuit.

To summarize all the key designed parameters, Table. 2 shows the key parameters and components used in this research. The rated value of the power switches are also stated in the table. In this study, the input voltage is set for 400 V, the input current will be 2.5 A. Conversely, the output voltage from the battery is set for 50 V, therefore, the current from the

TABLE 3. Specifications for key parameters of proposed converter.

Parameters	Specifications / Models
N_{high} : N_{low}	8 : 1
L_{eq1}	100 μH
C_{grid}	100 μF / 450 V
C_{bat}	470 μF / 100 V
$S_1 \sim S_4$	IPx60R280P6, 650 V/13 A
$S_5 \sim S_8$	IRFP4321PbF, 150 V/85 A
Digital signal controller	TMS320F28335
Isolated gate driver	TLP350
Duty ratio	48 %

(a). V_{GS8}:20V/div, V_{GS1}:20V/div, V_{DS1}:500V/div, I_{DS1}:2A/div, Time:5μs/div

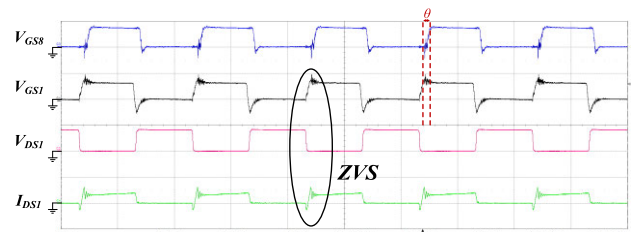(b). V_{high}:1kV/div, V_{low}:100V/div, I_{Lk1}:2A/div Time:5μs/div

FIGURE 26. Waveforms for G2V Mode at light load 100 W.

battery will be 20 A respectively. In addition, all the power switches at the high-voltage side and low-voltage side are MOSFET from Infineon Technologies. The specifications are also shown in Table 3. In the section II, the ideal duty ratio for operation principle analysis is set for almost 50 %. However, for the practical experiment, the dead time needs to be taken into consideration. The actual duty ratio is set for 48 % to avoid short circuit situation.

B. EXPERIMENTAL WAVEFORMS FOR G2V MODE

The following waveforms verify the proposed concept is feasible. As shown in Fig. 29, the proposed converter is operated in G2V mode at light load of 100 W. The input voltage is V_{grid}=400 V, and the output voltage is V_{bat}=50 V. Fig. 29(a) shows the phase-shift angle θ, driving signal and the current waveform of the power switch. Fig. 29(b) shows the V_{high}, V_{low}, and the current I_{Lk1} of the circuit.

As shown in Fig. 30, when the converter is operated in G2V mode for 600 W, the input voltage is V_{grid}=400 V, and the output voltage is V_{bat}=50 V. From Fig. 30(a), it can be observed that before the power switch S_1 is turned on, a reverse current I_{DS1} flows through the body diode. This reverse current allows the power switches to release the energy stored in the parasitic capacitance and thus the voltage

(a). V_{GS8}:20V/div, V_{GS1}:20V/div, V_{DS1}:500V/div, $_{DS1}$:5A/div, Time:5μs/div
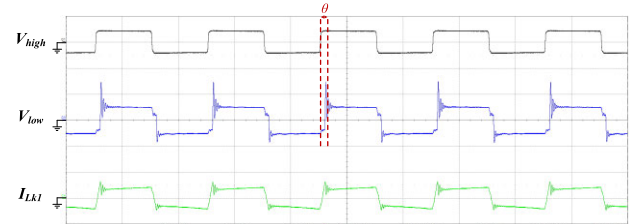
(b). V_{high}:1kV/div, V_{low}:100V/div, I_{Lk1}:5A/div, Time:5μs/div

FIGURE 27. Waveforms for G2V Mode at 600W.

V_{DS1} reduces to 0 V to achieve ZVS function. Fig. 30(b) shows the V_{high}, V_{low}, and the current I_{Lk1} of the circuit.

Fig. 31 shows the key waveforms when the converter is operated in G2V mode at full load, the input voltage is V_{grid}=400 V, and the output voltage is V_{bat}=50 V. It can be seen that from Fig. 31(a), before the power switch S_1 is turned on, the voltage V_{DS1} on the switch has been reduced to zero in advance to achieve the ZVS condition. Fig. 31(b) shows the V_{high}, V_{low}, and the current I_{Lk1} of the circuit with varying phase-shift angle θ.

C. EXPERIMENTAL WAVEFORMS FOR V2G MODE

In this section, the power flow is from the battery side to the DC grid side. As shown in Fig. 32, when the converter is operated in V2G mode at light load 100 W, the input voltage is V_{bat}=50 V, and the output voltage is the key waveform of V_{grid}=400 V. Fig. 32(a) shows the phase-shift angle θ, the driving signal and the current of the power switch. Fig. 32(b) shows the V_{high}, V_{low}, and the current I_{Lk1} of the circuit.

As shown in Fig. 33, when the converter is operated in V2G mode at 600 W for the output load, the input voltage is V_{bat}=50 V, and the output voltage is V_{grid}=400 V. Fig. 33(a) shows the phase-shift angle θ, the driving signal and the current of the power switch. Fig. 33(b) shows the V_{high}, V_{low}, and the current I_{Lk1} of the circuit.

As shown in Fig. 34, when the converter is operating in V2G mode at full load for 1 kW, the input voltage is V_{bat}=50 V, and the output voltage is V_{grid}=400 V. From these waveforms under different loading conditions, the magnitude of the power flow can be adjusted successfully.
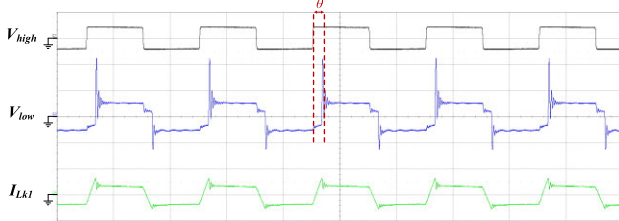
D. EFFICIENCY CURVES FOR G2V AND V2G

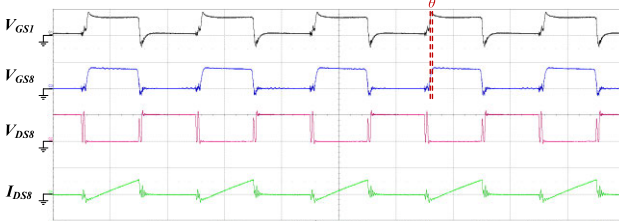Fig. 35 shows the efficiency curve of the proposed bidirectional converter when the converter works in the G2V mode,
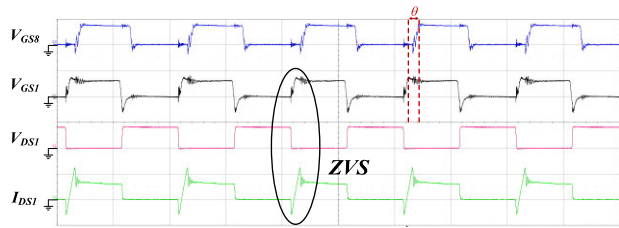
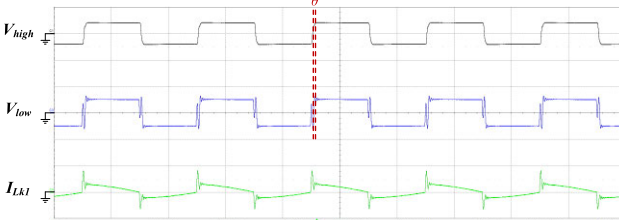(a). V_{GS8}:20V/div, V_{GS1}:20V/div, V_{DS1}:500V/div, I_{DS1}:5A/div、Time:5μs/div

(b). V_{high}:1kV/div, V_{low}:100V/div, I_{Lk1}:10A/div, Time:5μs/div

FIGURE 28. Waveforms for G2V Mode at 1 kW.

(a). V_{GS1}:20V/div, V_{GS8}:20V/div, V_{DS8}:50V/div, I_{DS8}:10A/div, Time:5μs/div

(b). V_{high}:1kV/div, V_{low}:100V/div, I_{Lk1}:2A/div, Time:5μs/div

FIGURE 29. Waveforms for V2G Mode at light load 100W.

(a). V_{GS1}:20V/div, V_{GS8}:20V/div, V_{DS8}:50V/div, I_{DS8}:20A/div, Time:5μs/div

(b). V_{high}:1kV/div, V_{low}:100V/div, I_{Lk1}:5A/div, Time:5μs/div

FIGURE 30. Waveforms for V2G Mode at 600W.

(a). V_{GS1}:20V/div, V_{GS8}:20V/div, V_{DS8}:50V/div, I_{DS8}:50A/div, Time:5μs/div
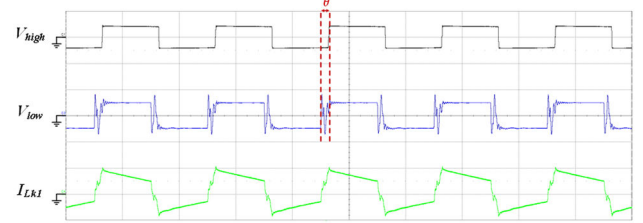
(b). V_{high}:1kV/div, V_{low}:100V/div, I_{Lk1}:5A/div, Time:5μs/div

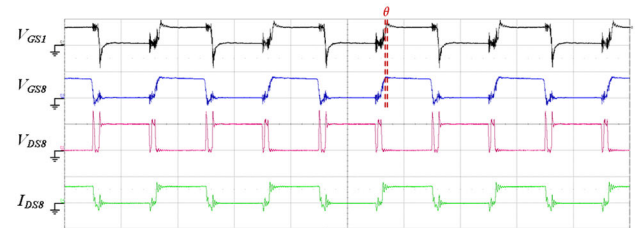**FIGURE 31.** Waveforms for V2G Mode at 1 kW.

the output voltage V_{bat} is 50V and the output load is increased from 100 W to 1 kW. The experimental results show that the highest efficiency of the G2V mode is 92.25 %.
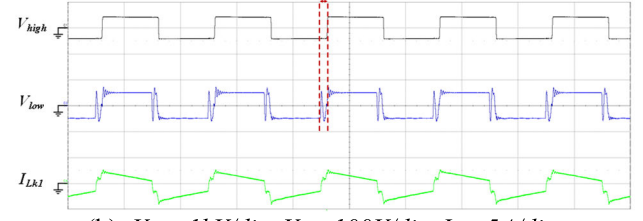
Fig. 33 shows the efficiency curve of the converter when the converter works in V2G mode, the output voltage V_{grid} is 400V, and the output load is also increased from 100 W to 1 kW. The experimental results show that the highest efficiency of the V2G mode is 93.02 %.

E. STRESS OF SWITCHES ANALYSIS FOR G2V AND V2G MODES
The proposed converter has eight power switches in the circuit. Therefore, the stress of the MOSFET at the high- voltage

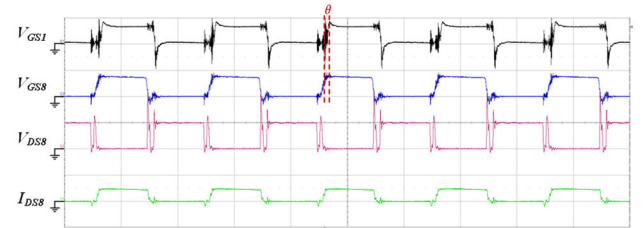

FIGURE 32. Efficiency curve of G2V mode.

and the low-voltage sides need to be considered. Referred to calculation from reference [25], the stress and power losses of switches, transformer and the auxiliary components can

FIGURE 33. Efficiency curve of V2G mode.

TABLE 4. Stress and power losses of switches.

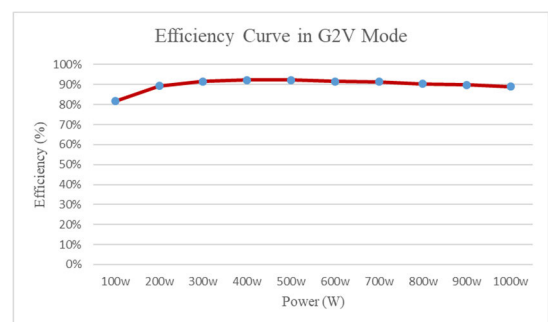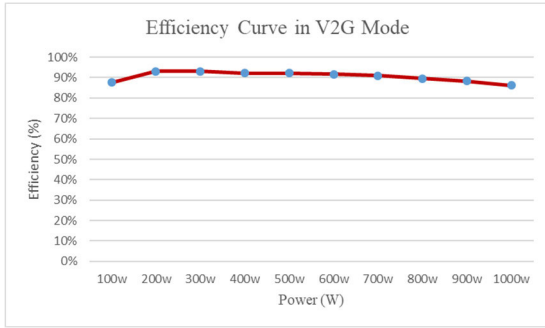| Items	Description	Voltage Stress	Current Stress	Conduction Losses
$S_1 \sim S_4$	At high-voltage side (DC grid) $R_{DS(ON)}$ = 280 mΩ	400 V_{dc}	2.5 A	1.75 W for each switch
$S_5 \sim S_8$	At low-voltage side (Battery) $R_{DS(ON)}$ =12 mΩ	50 V_{dc}	20 A	4.8 W for each switch

TABLE 5. The power losses of power switches, transformer and the auxiliary component.

Items	Description	losses
P_{SW}	Switching loss	1.57 W for 8 switches
$P_{Driving\_loss}$	C_{iss} loss of MOSFET stray capacitance	0.58 W for 8 switches
$P_{Turn\_off\_loss}$	C_{oss} loss of MOSFET stray capacitance	1.923 W for 8 switches
P_{core_loss}	Transformer core loss	0.003 W
P_{copper_loss}	Transformer copper loss	3.88 W

be obtained and summarized in Table. 4 and Table. 5. Both G2V and V2G modes are considered under full load 1 kW condition. In Table 4, the stray capacitors for C_{iss} and C_{oss} will dominate the driving loss and turn off loss of a power switch. During the driving procedure, the C_{iss} will be charged by V_{gs}. On the other hand, within the turn off duration, V_{DS} will charge to C_{oss}. The power loss of a switch can be analyzed in detail. Besides, the main transformer also plays an important role for this bidirectional converter. The core loss and the copper loss are stated in Table 5 as well.

F. PRACTICAL EXPERIMENTAL ENVIRONMENT SETUP
The proposed converter with high transformation ratio bidirectional converter and the testing equipments are shown in Fig. 34. In order to provide a clear components layout, the complete proposed prototype circuit of the power stage is also shown Fig. 35. Besides, the specification and the model of each instrument are listed in Table 6.
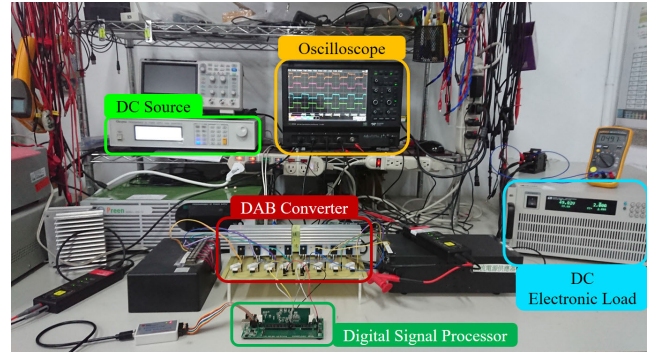

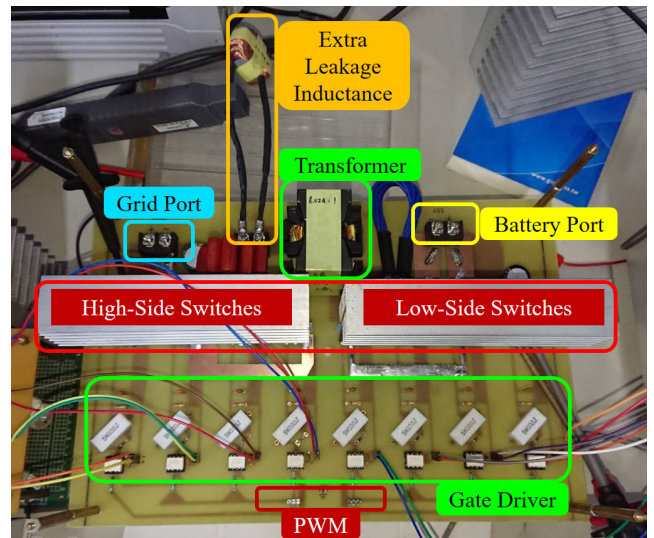**FIGURE 34.** Experimental environment and testing equipments.

FIGURE 35. Components layout of the proposed prototype circuit.

TABLE 6. Specifications of the testing instruments.

Specification of instruments	Model
DC power source, (600 V,8 A,1.2 kW)	Chroma_62024P-600-8
DC electronic load, (1.2 kV, 240 A, 6 kW)	ITECH IT8906E-1200-240
Oscillation scope, (4Ch, 200 MHz)	Lecroy_HDO4034
Voltage probe, (1.5 kV,100 MHz)	CYBERTEK_DP6150A
Current probe, (30 A, 50 MHz)	CYBERTEK_CP8030A
Digital multi-meter, (AC/DC, 10 A, 1 kV)	FLUKE_18B

VII. CONCLUSION
This study provides a complete design procedure and implements a bidirectional full-bridge phase-shift converter with high transformation ratio in detail. By improving the efficiency of the conventional phase-shift converter, the output-side rectifier diodes are replaced by power switches, and both sides of the drive signals are all triggered at the same time. This proposed scheme is suitable for high-low voltage ratio application. Based on the experimental results, both of G2V mode and V2G mode are verified by the measurements. The prototype of the bidirectional converter is implemented for 1 kW which can be used in electric scooters parking station in the near future. In the practical charging/discharging application, the charging system location, the penetration level, and

the charging time of electric vehicles will definitely influence the stability of the bidirectional power converter. Hence, the future scope of this work can be focused on the transient voltage regulation with high speed compensation techniques.

REFERENCES

[1] J. Hu, C. Ye, Y. Ding, J. Tang, and S. Liu, "A distributed MPC to exploit reactive power V2G for real-time voltage regulation in distribution networks," *IEEE Trans. Smart Grid*, vol. 13, no. 1, pp. 576–588, Jan. 2022.

[2] X. Bai and W. Qiao, "Robust optimization for bidirectional dispatch coordination of large-scale V2G," *IEEE Trans. Smart Grid*, vol. 6, no. 4, pp. 1944–1954, Jul. 2015.

[3] Z. Hu, K. Zhan, H. Zhang, and Y. Song, "Pricing mechanisms design for guiding electric vehicle charging to fill load valley," *Appl. Energy*, vol. 178, pp. 155–163, Sep. 2016.

[4] L. Jian, Y. Zheng, and Z. Shao, "High efficient valley-filling strategy for centralized coordinated charging of large-scale electric vehicles," *Appl. Energy*, vol. 186, pp. 46–55, Jan. 2017.

[5] D. Alahakoon and X. Yu, "Smart electricity meter data intelligence for future energy systems: A survey," *IEEE Trans. Ind. Informat.*, vol. 12, no. 1, pp. 425–436, Feb. 2016.

[6] N. Saputro and K. Akkaya, "Investigation of smart meter data reporting strategies for optimized performance in smart grid AMI networks," *IEEE Internet Things J.*, vol. 4, no. 4, pp. 894–904, Aug. 2017.

[7] R. Moghaddass and J. Wang, "A hierarchical framework for smart grid anomaly detection using large-scale smart meter data," *IEEE Trans. Smart Grid*, vol. 9, no. 6, pp. 5820–5830, Nov. 2018.

[8] G. Fenza, M. Gallo, and V. Loia, "Drift-aware methodology for anomaly detection in smart grid," *IEEE Access*, vol. 7, pp. 9645–9657, 2019.

[9] M. M. Buzau, J. Tejedor-Aguilera, P. Cruz-Romero, and A. Gomez-Exposito, "Detection of non-technical losses using smart meter data and supervised learning," *IEEE Trans. Smart Grid*, vol. 10, no. 3, pp. 2661–2670, May 2019.

[10] Y. Wang, Q. Chen, T. Hong, and C. Kang, "Review of smart meter data analytics: Applications, methodologies, and challenges," *IEEE Trans. Smart Grid*, vol. 10, no. 3, pp. 3125–3148, May 2019.

[11] B. Zhao, S. Qiang, W. Liu, and Y. Sun, "Overview of dual-active-bridge isolated bidirectional DC–DC converter for high-frequency-link power-conversion system," *IEEE Trans. Power Electron.*, vol. 29, no. 8, pp. 4091–4106, Aug. 2014.

[12] W. Chen, P. Rong, and Z. Lu, "Snubberless bidirectional DC–DC converter with new CLLC resonant tank featuring minimized switching loss," *IEEE Trans. Ind. Electron.*, vol. 57, no. 9, pp. 3075–3086, Sep. 2010.

[13] Y. Du, S. Lukic, B. Jacobson, and A. Huang, "Review of high power isolated bi-directional DC–DC converters for PHEV/EV DC charging infrastructure," in *Proc. IEEE Energy Convers. Congr. Expo.*, Sep. 2011, pp. 553–560.

[14] B. Zhao, Q. Yu, and W. Sun, "Extended-phase-shift control of isolated bidirectional DC–DC converter for power distribution in microgrid," *IEEE Trans. Power Electron.*, vol. 27, no. 11, pp. 4667–4680, Nov. 2012.

[15] B. Zhao, Q. Yu, and W. Sun, "Bidirectional full-bridge DC–DC Converters with dual phase-shifting control and its backflow power characteristic analysis," *Proc. CSEE*, vol. 32, no. 12, pp. 43–50, 2012.

[16] S. Chaurasiya, N. Mishra, and B. Singh, "A 50 kW bidirectional fast EV charger with G2V & V2G/V2V capability and wide voltage range," in *Proc. IEEE 5th Int. Conf. Comput. Commun. Autom. (ICCCA)*, Oct. 2020, pp. 652–657.

[17] J. Hu, S. Cui, and R. W. De Doncker, "Natural boundary transition and inherent dynamic control of a hybrid-mode-modulated dual-active-bridge converter," *IEEE Trans. Power Electron.*, vol. 37, no. 4, pp. 3865–3877, Apr. 2022.

[18] F. D. Esteban, F. M. Serra, and C. H. De Angelo, "Control of a DC–DC dual active bridge converter in DC microgrids applications," *IEEE Latin Amer. Trans.*, vol. 19, no. 8, pp. 1261–1269, Aug. 2021.

[19] C. Sun, X. Zhang, J. Zhang, M. Zhu, and J. Huang, "Hybrid input–series–output-series modular DC–DC converter constituted by resonant and nonresonant dual active bridge modules," *IEEE Trans. Ind. Electron.*, vol. 69, no. 1, pp. 1062–1069, Jan. 2022.

[20] J. Deng and H. Wang, "A hybrid-bridge and hybrid modulation-based dual-active-bridge converter adapted to wide voltage range," *IEEE J. Emerg. Sel. Topics Power Electron.*, vol. 9, no. 1, pp. 910–920, Feb. 2021.

[21] Q. Bu, H. Wen, and J. Wen, "Optimized transient modulation control of bidirectional full-bridge DC–DC converter," in *Proc. 10th Int. Conf. Power Electron. ECCE Asia*, May 2019, pp. 3102–3107.

[22] V. Jeyakarthikha and K. R. Vairamani, "Multiport bidirectional DC–DC converter for energy storage applications," in *Proc. Int. Conf. Circuits, Power Comput. Technol.*, Mar. 2014, pp. 411–417.

[23] P. Das, S. A. Mousavi, and G. Moschopoulos, "Analysis and design of a nonisolated bidirectional ZVS-PWM DC–DC converter with coupled inductors," *IEEE Trans. Power Electron.*, vol. 25, no. 10, pp. 2630–2641, Oct. 2010.

[24] R. G. Gago, S. F. Pinto, and J. F. Silva, "G2V and V2G electric vehicle charger for smart grids," in *Proc. IEEE Int. Smart Cities Conf. (ISC2)*, Sep. 2016, pp. 1–6.

[25] Y. Shen, W. Zhao, Z. Chen, and C. Cai, "Full-bridge LLC resonant converter with series-parallel connected transformers for electric vehicle on-board charger," *IEEE Access*, vol. 6, pp. 13490–13500, 2018.

SEN-TUNG WU was born in Taipei, Taiwan, in 1980. He received the B.S., M.S., and Ph.D. degrees from the Department of Electronic and Computer Engineering, National Taiwan University of Science and Technology, Taiwan, in 2003, 2005, and 2014, respectively. He had working experience with the Research and Development Department of switching power supply design manufacture for several years. In 2017, he was an Assistant Professor with the Department of Electrical Engineering, National Formosa University, Yunlin, Taiwan. He has been an Associate Professor with the EE Department, since 2022. His main research interests include power electronics, energy converter designs, battery chargers, bidirectional converters, power factor correction circuit design, and wireless power transfer applications.

BO-YU YANG is from Keelung, Taiwan. He received the B.S. and M.S. degrees from the Department of Electrical Engineering, National Formosa University, Yunlin, in 2019 and 2021, respectively. He has been working with LITE-ON Technology Company, Taiwan, as an EE Research and Development Engineer, since 2021. His research interests include power electronics and bidirectional converter design and circuit analysis.